A novel aluminium/CFRP hybrid composite with a bio-inspired crossed-lamellar microstructure for preservation of structural integrity

R. Häsä[a,*], S. T. Pinho[a]

[a]*Department of Aeronautics, Imperial College London, South Kensington Campus, London SW7 2AZ, United Kingdom*

Abstract

In this paper, we demonstrate that a novel hybrid composite of aluminium and Carbon Fibre Reinforced Polymer (CFRP) with a microstructure inspired by a biological crossed-lamellar microstructure is an attractive alternative for applications where structural integrity is paramount. Composites with such microstructure are prototyped and tested using both standard and thin-ply CFRP prepreg. Three-point bend tests are carried out in an SEM environment, showing extensive diffuse damage in the CFRP and yielding in the aluminium. This is the first hybrid crossed-lamellar-inspired microstructure in the literature and the results demonstrate that this novel microstructure can be loaded up to record large curvatures (in comparison with other CFRPs and hybrid CFRPs) while retaining its structural integrity and dissipating energy under stable conditions.

Keywords: Carbon fibres (A), Hybrid composites (A), Fracture (B), Damage tolerance (C), Biomimetics

1. Introduction

The ability of components to preserve their structural integrity is paramount in various applications in the aerospace and automotive industries, including, e.g., nacelles, leading edges of aircraft wings and components that are subject to side pole impact.

*Corresponding author

Email address: r.hasa15@imperial.ac.uk (R. Häsä)

At the same time, requirements for weight savings have driven these industries towards extensive use of CFRPs in their designs. However, CFRPs are inherently brittle and suffer from low damage tolerance, making them susceptible to impact damage.

Recent research has shown that these seemingly contradictory design requirements can be met through careful microstructural design, with a focus on designs that aim at enhancing the damage tolerance of CFRPs [1–4]. Nature provides an excellent source of inspiration for these novel microstructures, since microstructures found in natural composites (e.g., bone, wood and mollusc shells) have evolved to preserve their structural integrity under attacks of predators. These natural microstructures diffuse damage through various strategies, making them more damage tolerant than their often relatively weak and brittle main constituents [5].

One microstructure found in nature that has evolved to resist impacts is the crossed-lamellar microstructure found, e.g., in the *Strombus gigas* shell (Figure 1). The crossed-lamellar microstructure varies slightly between different species, and it has been experimentally characterised in the literature [6] in bending [7–10], compression [9, 11, 12] and indentation [13]. Much of the research focuses on the *Strombus gigas* shell (Figure 1(a)), studying its behaviour under bending and compression [14–17] and characterising its microstructure using nanoindentation [18, 19], optical methods [20, 21] and biochemical characterisation [22].

Despite consisting 99.9 w% of brittle aragonite [17], the toughness of the *Strombus gigas* shell is up to four orders of magnitude higher than the toughness of monolithic aragonite [15]. The toughness of the shell arises from its microstructure, that can be seen on the fracture surface of the shell in Figure 1(b), and is schematically illustrated in Figure 1(c). On the coarsest length scale, the microstructure consists of three macroscopic layers with $0°/90°/0°$ orientation [15]. These layers are identified as inner, middle and outer layers and marked I, M and O, respectively, in Figures 1(b) and 1(c). The macroscopic layers further comprise 1^{st} order lamellae with $\pm 35°$ to $\pm 45°$ orientation with respect to the thickness of the shell, and these 1^{st} order lamellae consist of 2^{nd} and 3^{rd} order lamellae (not illustrated in Figure 1(c)) on smaller length scales.

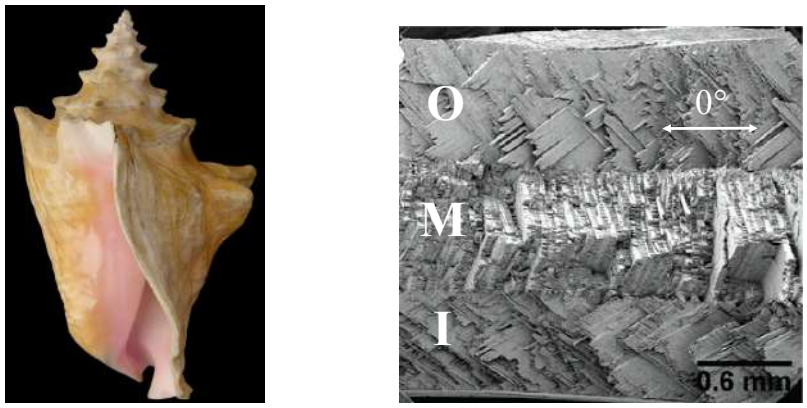

(a) (b)

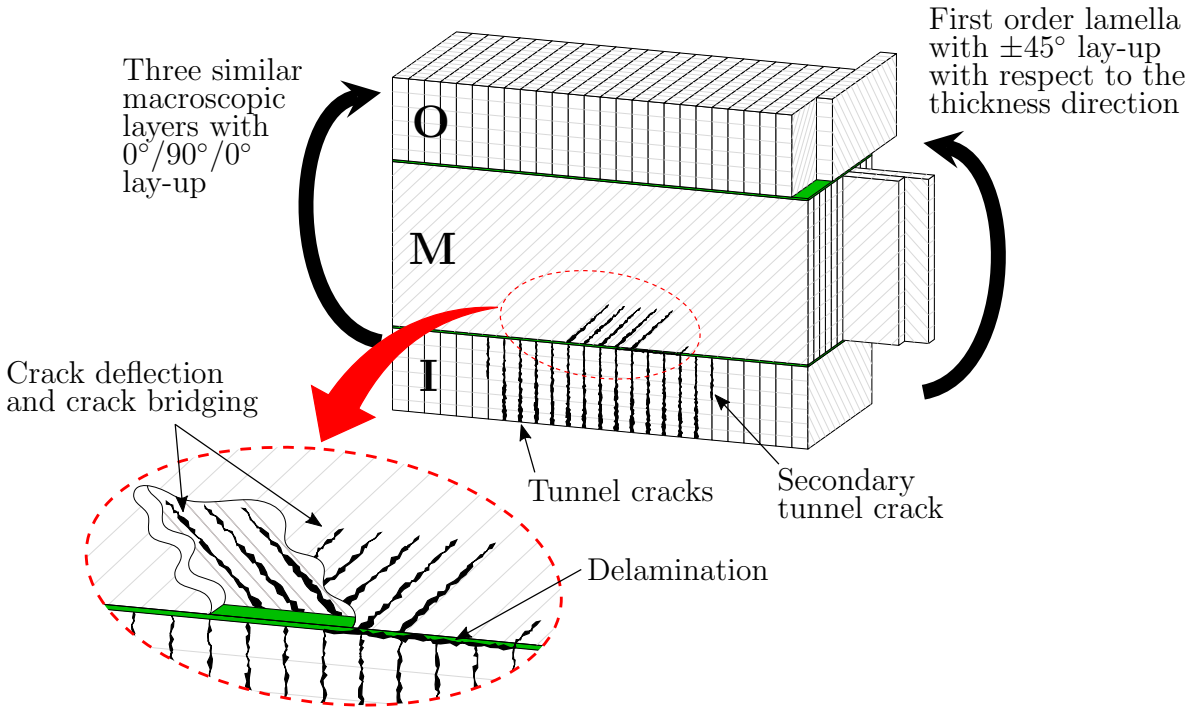

(c)

Figure 1: (a) The *Strombus gigas* shell [23] has a crossed-lamellar microstructure, as seen; (b) on the fracture surface of the shell (adapted with permission from Su et al. [20]. Copyright 2004 American Chemical Society) and; (c) in a schematic illustration of the microstructure (not to scale). The most important toughening mechanisms in the crossed-lamellar microstructure are parallel tunnel cracking in the inner layer, subsequent crack deflection in the middle layer, and crack bridging, debonding and sliding of the middle layer lamellae. Adapted from [4].

Under bending loads, the crossed-lamellar microstructure dissipates energy through various mechanisms [24], with the main toughening mechanisms schematically illustrated in Figure 1(c). First, parallel tunnel cracks form between the 1st order lamellae

on the tensile side (i.e., the inner layer) and they subsequently arrest at the interface between the inner and middle layers. The cracks then deflect to grow along the ±45° direction in the middle layer, and they are bridged because the preferred crack growth direction alternates 90° between the adjacent lamellae. Eventually, the lamellae debond and slide against each other, which leads to large fracture surfaces and energy dissipation through friction.

Although crossed-lamellar microstructures are abundant in nature, they have not yet been widely exploited in synthetic materials, with only a few examples reported in the literature using ceramics [25, 26], silicon [27], bamboo [28] and polymer-based materials [4, 29, 30]. In fact, ASTM [31] allows for a ±45° lay-up with respect to thickness to be be used to determine the shear properties of composite materials, but no work in the literature has used such lay-up in CFRP within a structural hybrid composite.

In the only CFRP microstructure mimicking the *Strombus gigas* shell in the literature [4], it was found that the middle layer dissipated a very significant amount of energy, and that the inner layer eventually caused localisation of failure due to the propagation of tunnel cracks (see Figure 2). It can be concluded from the work in [4] that preventing damage localisation in the inner layer is fundamental for a crossed-lamellar microstructure that aims for preserving its structural integrity.

Given the state of the art, in this work we propose, for the first time in the literature,

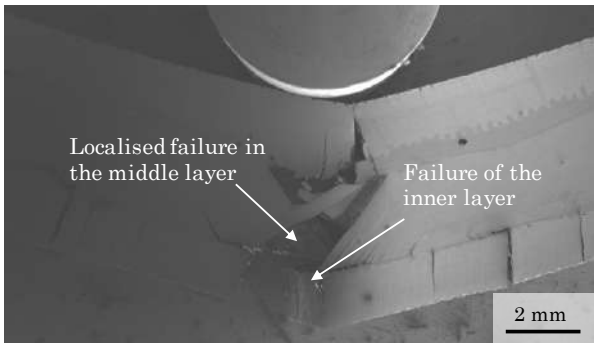

Figure 2: In a CFRP with a crossed-lamellar microstructure, failure of the inner layer leads to localised failure of the middle layer (adapted from Häsä and Pinho [4]).

a hybrid metal/crossed-lamellar composite; it exploits the excellent damage diffusion capability of the middle layer of the crossed-lamellar CFRP, and ductility of aluminium in the inner and outer layers. The energy available for delamination between the $\pm 45°$ plies in the middle layer depends on the thickness of the prepreg used. For this reason, in Section 2 we prototype the composite using two different families of prepreg with different ply thicknesses. In Section 4, we demonstrate that this hybrid composite has a unique mechanical response, it can be loaded up to record large curvatures while retaining its structural integrity through damage diffusion, and that it therefore has potential for step changes in the design of containment structures and other structures that require high damage tolerance.

2. Methods

2.1. Microstructure definition

An original bio-inspired hybrid microstructure was conceived as a result of an iterative prototyping process, whereby a crossed-lamellar CFRP layer was sandwiched between 0.4 mm thick 2024-T3 aluminium (see Figure 3). The aluminium was chosen due to its attractive mechanical properties and its prevalence in other fibre metal laminates [32]. Earlier iterations of the hybrid crossed-lamellar microstructures are given in Appendix A.

The novel aluminium/CFRP hybrid was prototyped using two different families of prepreg – standard-ply prepreg Hexcel IM7/8552 and thin-ply prepreg SkyFlex USN020A. The thickness of crossed-lamellar CFRP middle layer was based on a parametric study conducted within the design of the first CFRP with a crossed-lamellar microstructure [4], as well as on manufacturing conditions.

2.2. Prototyping

To manufacture the crossed-lamellar CFRP layer (the middle layer in the hybrid composite in Figure 3), two laminates with 10 mm nominal thickness and a symmetric layup sequence $[+45°/-45°]_{n\mathrm{S}}$ (where $n = 20$ and the nominal thickness of the prepreg

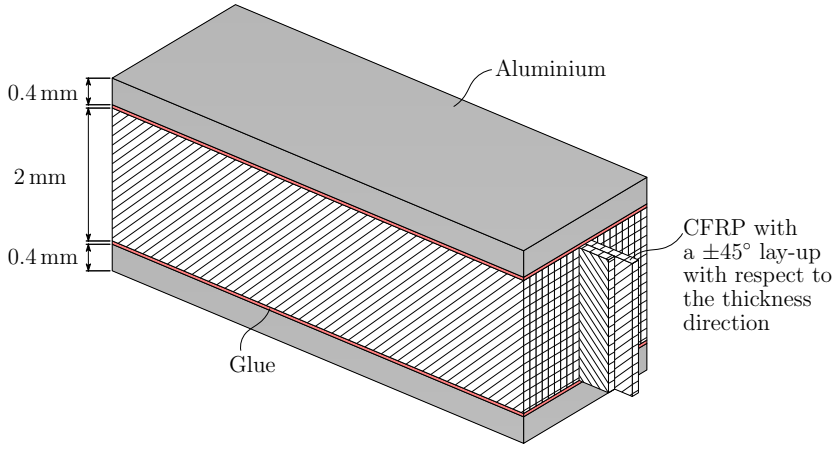

Figure 3: A schematic figure of the prototyped crossed-lamellar microstructure with aluminium inner and outer layers.

is 125 μm for the standard-ply prepreg, and $n = 100$ and the nominal thickness of the prepreg is 25 μm for the thin-ply prepreg) was manufactured. The laminates were cut into 3 mm wide slices and further ground to 2 mm to ensure flat and even surfaces. The slices were subsequently rotated so that the fibre orientation angle was now with respect to the thickness direction, as detailed in [4], and put in place ready for bonding.

The surface of the aluminium was grit-blasted and etched in chromic acid according to the guidelines originally outlined by Forest Product Laboratory [33]. During the etching, the aluminium was first submerged in 68 °C acid solution for 20 minutes and subsequently rinsed under running water for 20 minutes.

The CFRP slices and the two aluminium sheets were bonded together using 3M ScotchWeld 9323 B/A toughened epoxy adhesive in order to form the microstructures shown in Figures 3 and 4. The microstructures were then clamped and cured in 65 °C for two hours to accelerate the strength build-up according to the adhesive manufacturer's instructions.

2.3. Testing

One specimen from each prepreg type (hence two different microstructures with dimensions listed in Table 1) were tested in a three-point bending (3PB) configuration as schematically illustrated in Figure 4. The tests were carried out using a Deben

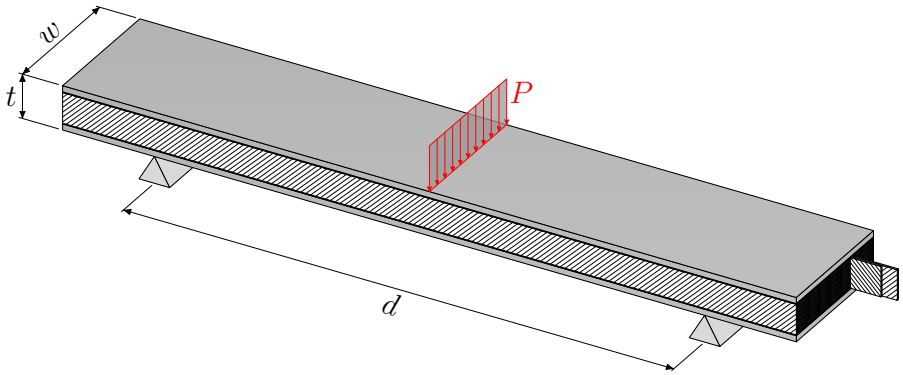

Figure 4: Sketch of the test set-up of the three-point bending test showing the dimensions and the testing orientation of the specimen.

Microtest Module with a 5 kN load cell with in-situ SEM. In order to enhance the quality of the SEM images, the specimens were polished and gold-sputtered on the side surface prior to testing.

The specimens were loaded at a displacement rate of 0.2 mm/min, and the test data was recorded at an acquisition rate of 200 ms. The displacements were read from the built-in extensometer and subsequently corrected to account for the compliance of the test rig.

The tests were run discontinuously in order to capture SEM images. At the beginning of the test, before major damage was observed, the displacement was held at load intervals of 50 N. At a later stage, when the damage was growing, the tests were paused at regular displacement intervals of 0.25 mm.

Table 1: Dimensions of the tested specimens with a crossed-lamellar middle layer and aluminium skins.

Specimen	d [mm]	t [mm]	w [mm]
Standard-ply	36	2.8	9.2
Thin-ply	36	2.9	9.3

3. Results

Figure 5 shows selected SEM images of the standard-ply and thin-ply microstructures taken during the test. The corresponding instances are annotated in the normalised load vs displacement curves in Figure 6. The load P was normalised by the second moment of area I, and the displacement δ was normalised by the thickness of the specimen t. The load drops in the curves are associated with specimen relaxation when the displacements were held to capture SEM images.

Figures 5(a) and (b) show the intact standard-ply and thin-ply specimens, respectively, prior to testing with the aluminium and CFRP layers highlighted. The progressive failure of the specimens is illustrated in Figures 5(c)-(h).

At an early stage of the test, an array of deflected cracks formed on the CFRP layer of the standard-ply microstructure (Figure 5(c)), while no cracks were observed on the thin-ply microstructure (Figure 5(d)), as also seen in Figures 7(a) and (b), showing a more detailed view of the standard-ply and thin-ply microstructures, respectively.

At a later stage of the tests, the cracks on the standard-ply specimen had slightly opened (Figure 5(e)), while no macroscopic damage was observed in the thin-ply specimen (Figure 5(f)).

The tests were stopped when the tester reached its maximum displacement. At the end of the test, the standard-ply specimen exhibited diffuse damage with an array of splits in the fibre direction in the middle layer (Figure 5(g) and a more detailed view in Figures 7(c) and (e)). A close-up of the splits (Figure 7(e)) shows that the cracks grew in the fibre direction with no visible broken fibres. Furthermore, shear cusps formed on the crack faces. Some degree of degradation was observed at the interface between the adhesive and the CFRP.

At the end of the test, the thin-ply specimen did not have macroscopic cracks visible on its surface (Figure 5(h)). However, a more detailed view of the specimen (Figures 7(d) and (f)) reveals minor splits in the CFRP, some broken fibres on the surface of the specimen, and degradation of the adhesive interface.

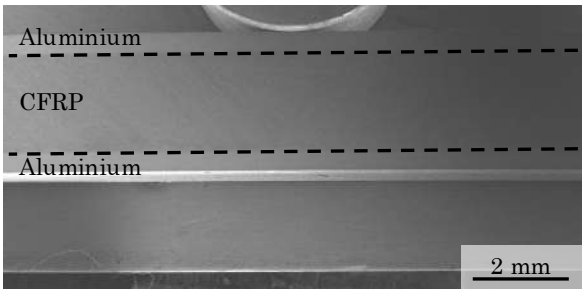

(a) $\delta/t = 0$, standard-ply

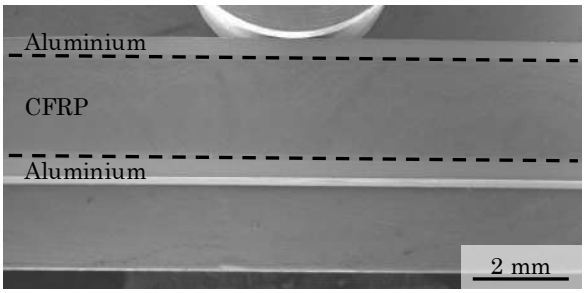

(b) $\delta/t = 0$, thin-ply

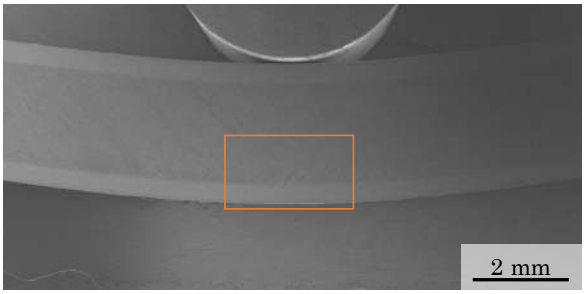

(c) $\delta/t = 0.9$, standard-ply

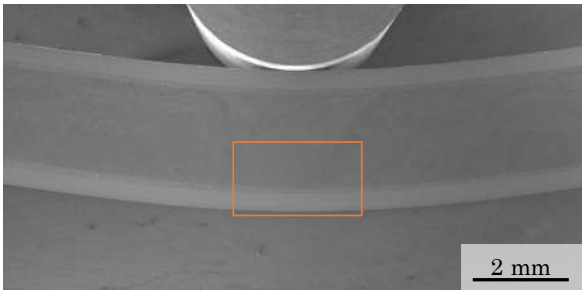

(d) $\delta/t = 0.9$, thin-ply

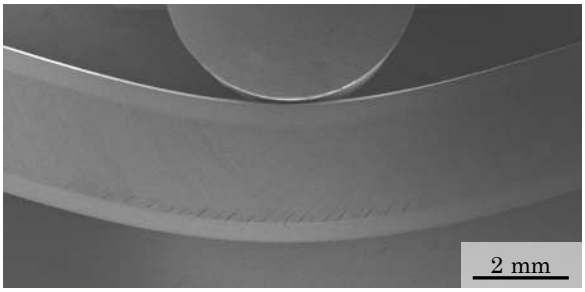

(e) $\delta/t = 1.9$, standard-ply

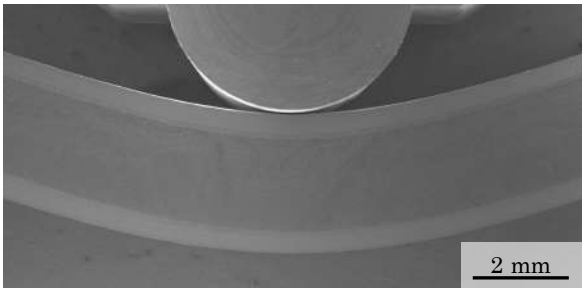

(f) $\delta/t = 1.9$, thin-ply

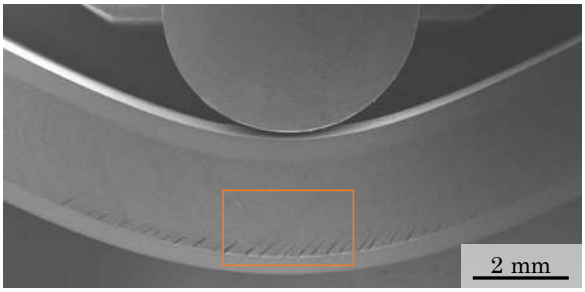

(g) $\delta/t = 2.7$, standard-ply

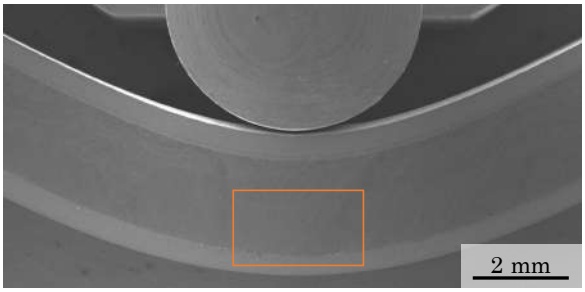

(h) $\delta/t = 2.8$, thin-ply

Figure 5: SEM images showing the standard-ply and thin-ply microstructures during the test at the instances annotated in Figure 6. Close-ups of the enclosed areas in Figures 5(c), (d), (g) and (h) are shown in Figure 7.

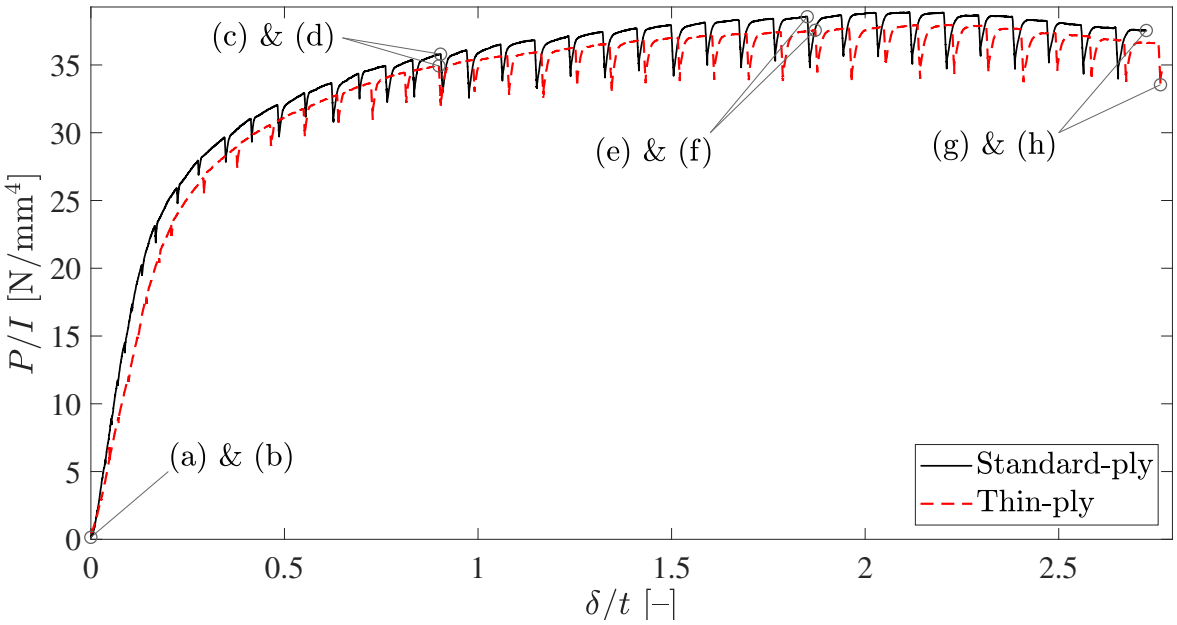

Figure 6: Normalised load vs displacement curves of the microstructures. The load P is normalised by the second moment of area I and the displacement δ is normalised by the thickness of the specimen t.

The microstructures dissipated energy in a stable manner, under increasing or constant load, as seen in the load vs displacement curves in Figure 6. Both microstructures exhibited similar behaviour, with the response of the standard-ply microstructure being slightly stiffer than that of the thin-ply microstructure.

After the tests, the damage in the specimens was assessed using an optical microscope (Figure 8). The specimens were ground and polished to the mid-plane first along the width of the specimen (plane A in Figure 8(a)) and then along the length of the specimen (plane B in Figure 8(a)). The micrographs of the standard-ply and thin-ply microstructures along these planes are shown in Figures 8(b) and (d), and Figures 8(c) and (e), respectively.

The standard-ply microstructure had kink band -type features with fibre failure, as seen in Figure 8(b), and matrix cracks (i.e., splits) along the fibre direction at various locations (Figure 8(d) with an example of a typical split enclosed in the figure). These splits were arrested at the $\pm 45°$ ply interfaces, and no delaminations were observed between the plies.

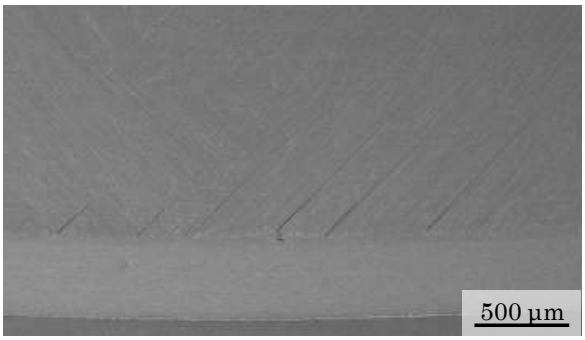

(a) $\delta/t = 0.9$, standard-ply

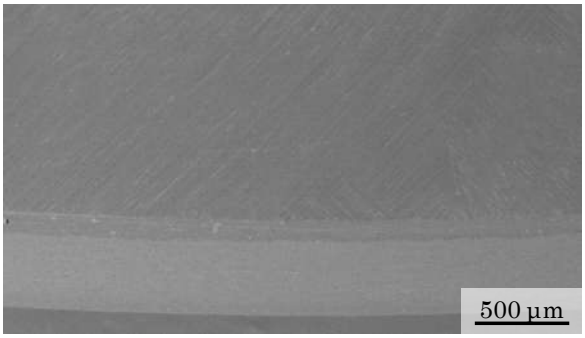

(b) $\delta/t = 0.9$, thin-ply

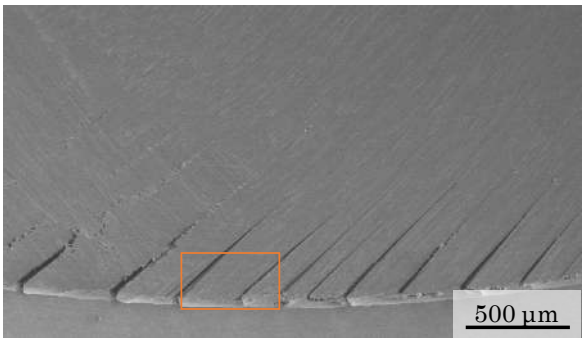

(c) $\delta/t = 2.7$, standard-ply

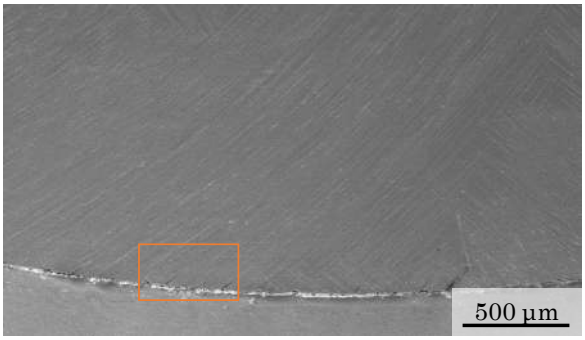

(d) $\delta/t = 2.8$, thin-ply

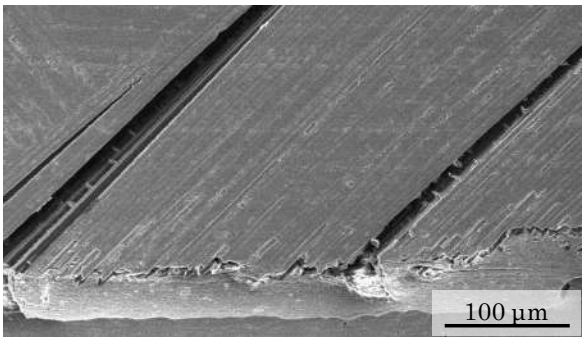

(e) $\delta/t = 2.7$, standard-ply

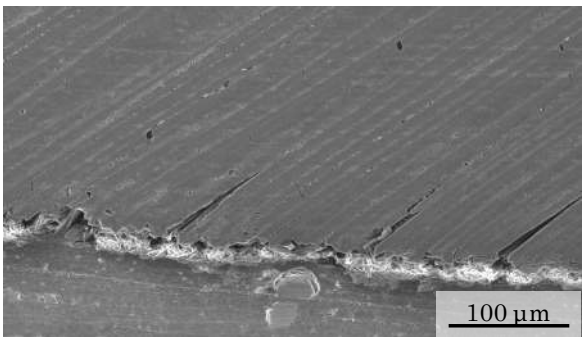

(f) $\delta/t = 2.7$, thin-ply

Figure 7: Details of the 3PB tests of the hybrid aluminium/CFRP microstructures. Figures 7(a)-(d) are details of the enclosed areas in Figure 5, and Figures 7(e) and (f) are details of Figures 7(c) and (d), respectively.

The thin-ply microstructure had fibre failure, but no visible fibre kinking (Figure 8(c)). The thin-ply microstructure did not exhibit splits along the fibre direction or delamination at the $\pm 45°$ ply interfaces (Figure 8(e)).

The curvature of the specimens while still under load at the end of the tests was

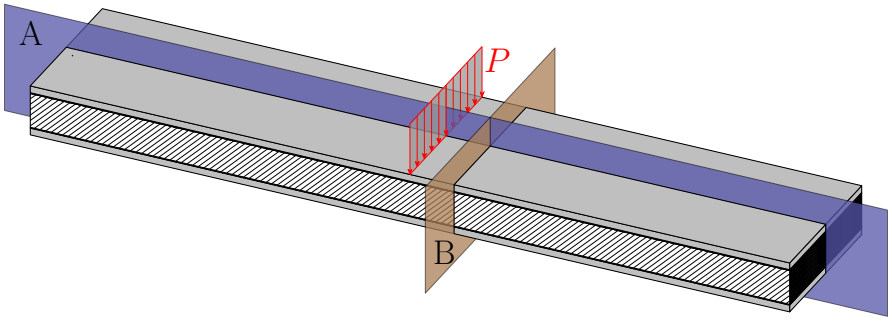

(a) Observation planes

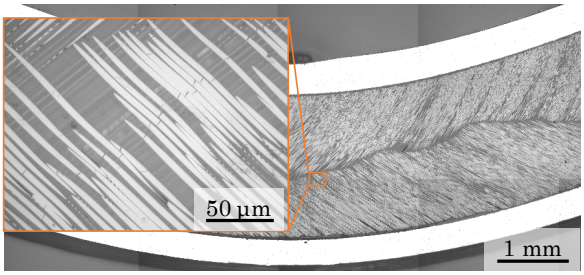

(b) Plane A, standard-ply

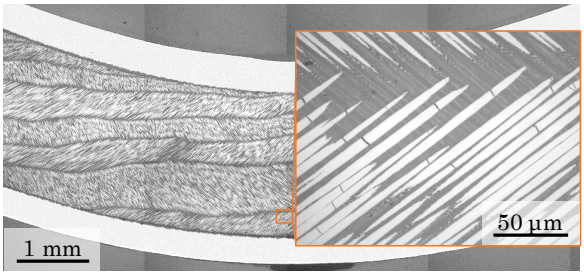

(c) Plane A, thin-ply

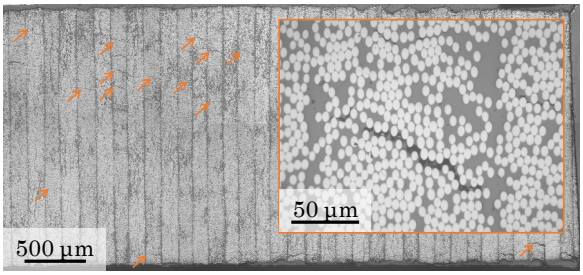

(d) Plane B, standard-ply

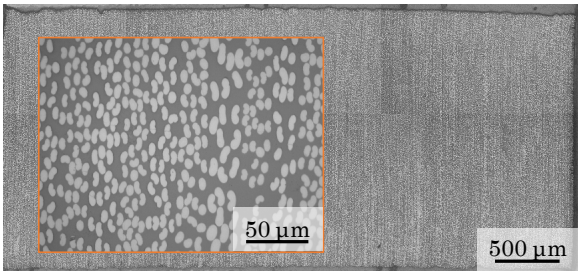

(e) Plane B, thin-ply

Figure 8: Post-mortem micrographs of the tested microstructures.

measured from the SEM images and is listed in Table 2. The elastic bending stiffness was also determined from the test data by calculating the slope of the elastic region of the load vs deflection curves and converting it to the bending stiffness using Euler-Bernoulli beam theory and the specimen dimensions. The density of the specimens was determined from the dimensions and mass of the specimens, and the elastic bending stiffness was finally normalised by the specific density of the material (see Table 2).

4. Discussion

4.1. Mechanical response

Two hybrid aluminium/CFRP composites with crossed-lamellar microstructures were successfully prototyped using two different families of prepreg. The consolidation in the CFRP layers was good, with no voids visible in the microstructures (see Figure 9).

Furthermore, although carbon fibre can induce galvanic corrosion in aluminium in direct contact, the adhesive acts as an isolator between these materials and may therefore hinder the occurrence of corrosion. To fully eliminate the risk of corrosion, other material systems could also be considered for such hybrid microstructures, such as aluminium/glass fibre reinforced polymer or titanium/CFRP.

Both microstructures exhibit similar mechanical behaviour (Figure 6). The stiffer response of the standard-ply microstructure can be attributed to the stiffer mechanical properties of the standard-ply prepreg [4]. The standard-ply prepreg is 1.6 times stiffer than the thin-ply prepreg (when comparing the E_{11} values); accordingly the elastic stiffness of the standard-ply microstructure is 1.53 times higher than the stiffness of the thin-ply microstructure.

The microstructures are able to undergo extremely large deformations ($\kappa > 0.1\,\mathrm{mm}^{-1}$)

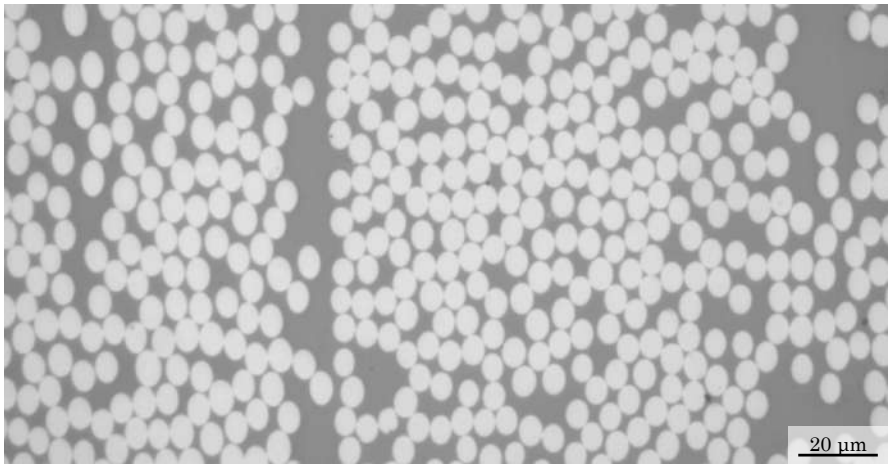

Figure 9: A representative micrograph of the standard-ply microstructure shows good consolidation and negligible void content in the cured CFRP.

without losing their load-carrying capacity. The microstructures preserve their structural integrity while dissipating energy under nearly constant load (Figure 6) through plastic deformation of the aluminium and damage diffusion in the middle CFRP layer.

The damage diffusion in the CFRP layer for both, the standard-ply microstructure and the thin-ply microstructure, manifests as a regular array of splits along the fibre direction (Figures 7(c) and (d)). In both microstructures, the growth of these splits in the middle layer was hindered due to the bridging effect of the $\pm 45^\circ$ architecture of the middle layer.

In the thin-ply microstructure, the damage in the middle layer is less visible than in the standard-ply microstructure (Figure 7(d) vs 7(c)). The difference in behaviour between the standard-ply and thin-ply specimens may be related both to the increased in-situ shear and transverse strengths in the thin-ply material, and to the fact that a small amount of local delamination is beneficial for the splits to open, but the energy available to grow a delamination is substantially lower for the thin-ply microstructure.

The post-mortem investigation of the standard-ply microstructure revealed kink bands and splits along the fibre direction (Figures 8(b) and (d)). The mechanism that we hypothesise to lead to the formation of the kink bands is schematically illustrated in Figure 10 and can be described as follows:

1. splits form at the bottom of the middle CFRP layer due to the tensile bending stress and subsequently propagate upwards at $\pm 45^\circ$ angle depending on the respective ply orientation (Figures 10(a) and (b));
2. since the splits are at $\pm 45^\circ$, and they are due to the tensile loading stresses in the

Table 2: The curvature of the specimens at the end of the tests, their density and specific elastic bending stiffness.

Specimen	κ [mm^{-1}]	ρ [g/cm^3]	$EI/\bar{\rho}$ [GPa mm^4]
Standard-ply	0.103	1.93	582.6
Thin-ply	0.102	1.96	419.8

horizontal direction, they grow under combined tension and shear in the material coordinate system, see Figures 10(a) and (c);

3. in the absence of delamination at the ±45° ply interfaces, as the split grows upwards (e.g. in a +45° ply, see Figure 10(a)), the adjacent plies are loaded in shear in the vicinity of the split (Figure 10(c)) and this shear leads to the formation of a kink band (Figure 10(d)). These kink bands are visible in the optical micrographs, see Figure 10(e).

For the thin-ply microstructure, the mechanism is the same. However, as mentioned before, since the in-situ transverse and shear strengths of the thin-plies are significantly higher and the driving force for delamination lower, one would expect that, for a given applied curvature, the ±45° splits are less developed and, concomitantly, the kink bands are less developed too. Both expectations can be observed in practice (see Figures 7(f) and 8(c)). The different fibre size and morphology, as seen in Figures 8(d) and (e), may also contribute to the difference in the observed damage on the specimens.

Both microstructures can be loaded up to large curvatures (Figures 5(g) and (h)

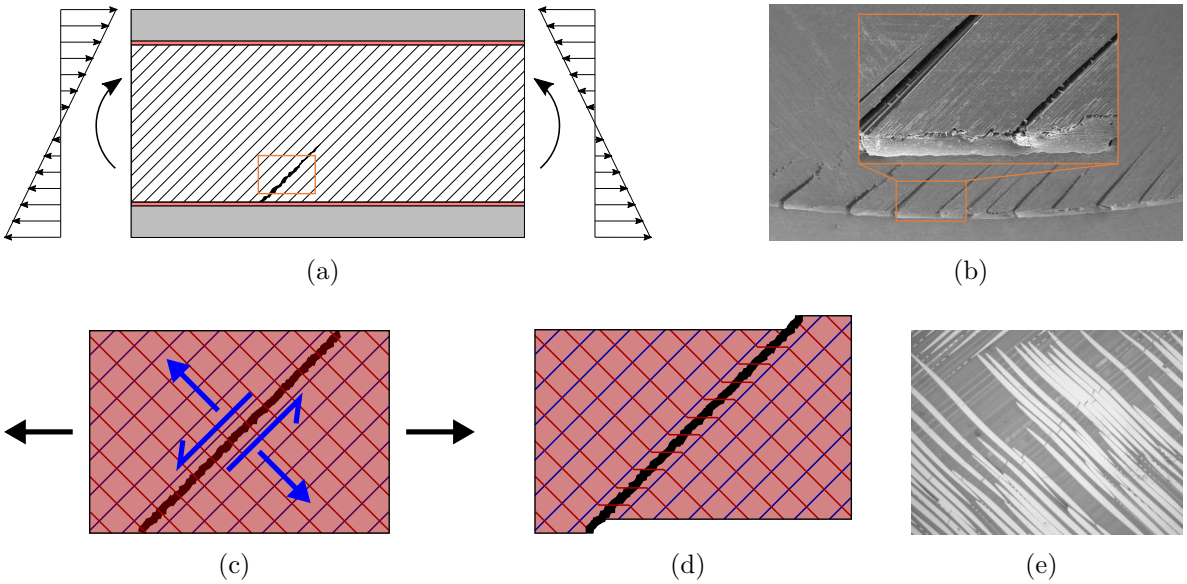

Figure 10: The mechanism leading to the formation of kink bands in the standard-ply microstructure.

and Table 2). Figure 11 shows the specific bending stiffness and the curvature at the end of the test of the hybrid CFRP microstructures, together with selected materials from the literature. The material properties of the selected materials are obtained from CES EduPack, apart from the values for the other aluminium/CFRP hybrids obtained from Dhaliwal and Newaz [34]. A beam with the same dimensions as our test specimens was used to obtain the bending stiffness and the curvature at failure.

The specific bending stiffnesses of the novel biomimetic hybrid microstructures are comparable to the stiffness of the other aluminium/CFRP hybrids and quasi-isotropic CFRPs, but the novel hybrid microstructures reach significantly larger curvatures than any of these materials.

Furthermore, compared with aluminium, the new hybrid microstructure with standard-ply prepreg is slightly stiffer than aluminium, whereas the thin-ply microstructure is

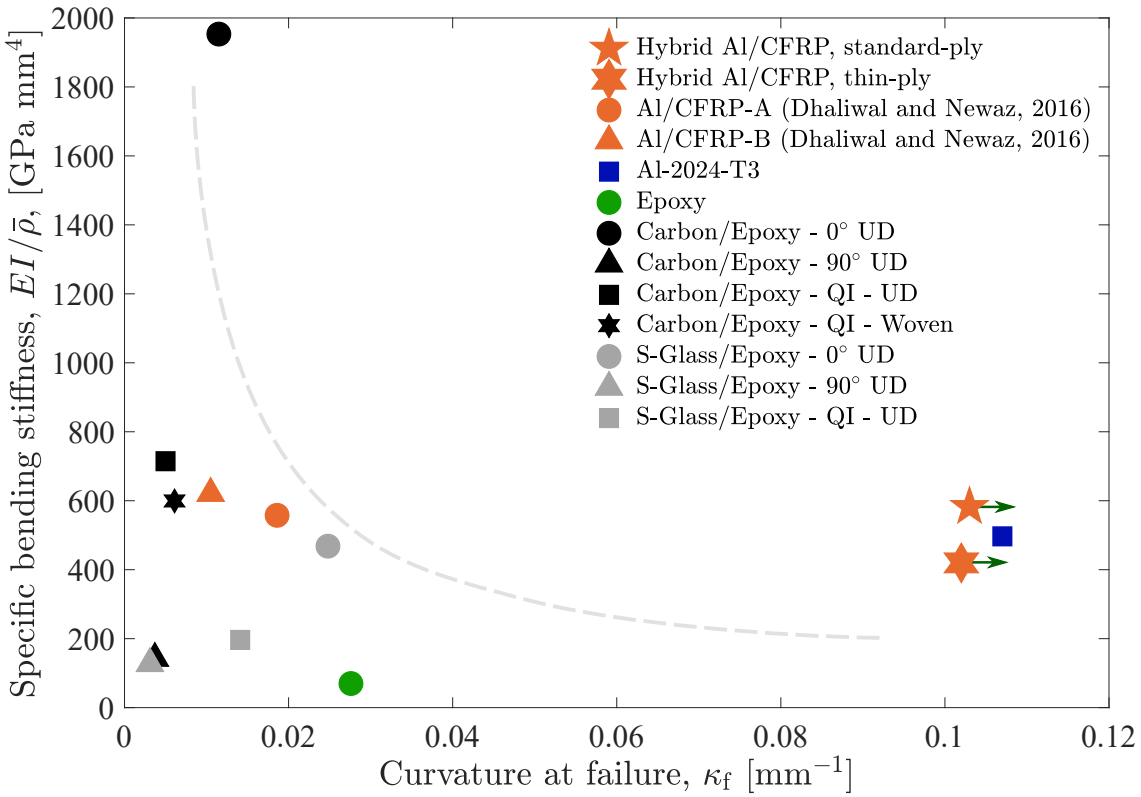

Figure 11: The specific bending stiffness and curvature at the end of the tests of the novel hybrid CFRP microstructures compared with selected materials.

slightly less stiff. The curvature of the novel hybrid microstructures at the end of the tests is slightly lower than the curvature at failure of aluminium. However, it should be noted that the tests were stopped prior to the final failure of the specimens (due to reaching the maximum displacement of the test rig), and no macroscopic failure is observed in the aluminium layers of these microstructures (Figures 5(g) and (h)). Therefore, it can be expected that the curvature at failure of the hybrid aluminium/CFRP microstructures most likely exceeds the curvature at failure of the aluminium when the microstructures are loaded until their final failure.

When compared with the CFRP and aluminium constituents, the analysis in the previous paragraph suggests that the hybrid microstructure proposed leads to a larger curvature to failure for a given bending stiffness, which suggests that hybrid crossed-lamellar microstructures exhibit a synergistic effect between the constituents. This is because the aluminium inner and outer layers provide cohesion for the splits in the crossed-lamellar CFRP layer and prevent them from opening, thus facilitating damage diffusion (Figure 2 vs Figure 5).

4.2. Numerical simulation

Since most of the energy dissipation occurs during a state of diffuse damage through the aluminium and the crossed-lamellar microstructure, without significant localisation of damage until the later stages of the test, we investigated whether the early stages of the mechanical response of the microstructures could be well reproduced using relatively simple numerical models with a non-linear mechanical response. The microstructures were modelled in Abaqus/Standard (version 2016) in 2D using CPE4R plane strain elements. The material properties of the CFRP (see Table 3) were homogenised using Classical lamination theory. The CFRP was modelled as having non-linear shear behaviour according to the Ramberg–Osgood model in the local 12-direction and was allowed to fail in shear using anisotropic perfect plasticity. We used a range of values from the literature [4, 35] for the maximum shear strength to account for the uncertainty in the in-situ effects, and a range of friction coefficients between the specimen and the

pins to estimate the effect of friction on the mechanical behaviour (see Figure 12).The aluminium was modelled as elastic-plastic material (see Table 3). In addition, the thin layer of adhesive between the CFRP and the aluminium was modelled using 0.05 mm thick CPE4R plane strain elements with properties given in Table 3.

The load and the support pins were modelled as analytical surfaces with hard contact in the normal direction and either frictionless contact or a contact with Coulomb friction governed by the coefficient μ in the tangential direction.

The Finite Element simulations (Figure 12) predict the mechanical behaviour of the microstructures reasonably well. The numerical results for the standard-ply microstructure predict the elastic stiffness of the microstructure accurately (Figure 12(a)), while the numerical results of the thin-ply microstructure slightly over-predict the stiffness (Figure 12(b)), suggesting that the values of the material parameters may have been slightly over-estimated.

Figure 12(c) shows the dissipated energy density in the crossed-lamellar region for the standard-ply microstructure with a shear strength $\tau_{\max} = 123\,\text{MPa}$ overlaid on an SEM image of the specimen at the end of the test. The figure shows an area of diffuse damage in the FE that matches relatively well with the area with visible damage in the experiments, with the most energy dissipated on the tension side under the load pin.

Table 3: The material properties used in the Finite Element model. The parameters E_{11}, E_{22} and E are elastic moduli, G_{12} is the shear modulus, ν_{12} and ν are Poisson's ratios, K and n are constants that define non-linearity in the Ramberg–Osgood model, σ^{y} is the yield strength and σ^{u} is the ultimate strength.

	E_{11} [GPa]	E_{22} [GPa]	G_{12} [GPa]	ν_{12} [–]	K [MPa]	n [–]
Standard-ply	164.0[36]	12.0[36]	4.6†	0.3[37]	258.0[38]	0.212[38]
Thin-ply	101.7[39]	6.0[40]	2.4[40]	0.2[40]	258.0†	0.212†

	E [GPa]	ν [–]	σ^{y} [MPa]	σ^{u} [MPa]
Al 2024-T3[41]	73.1	0.33	270	405
ScotchWeld 9323 B/A[42]	2.87	0.37	40†	–

† Assumed

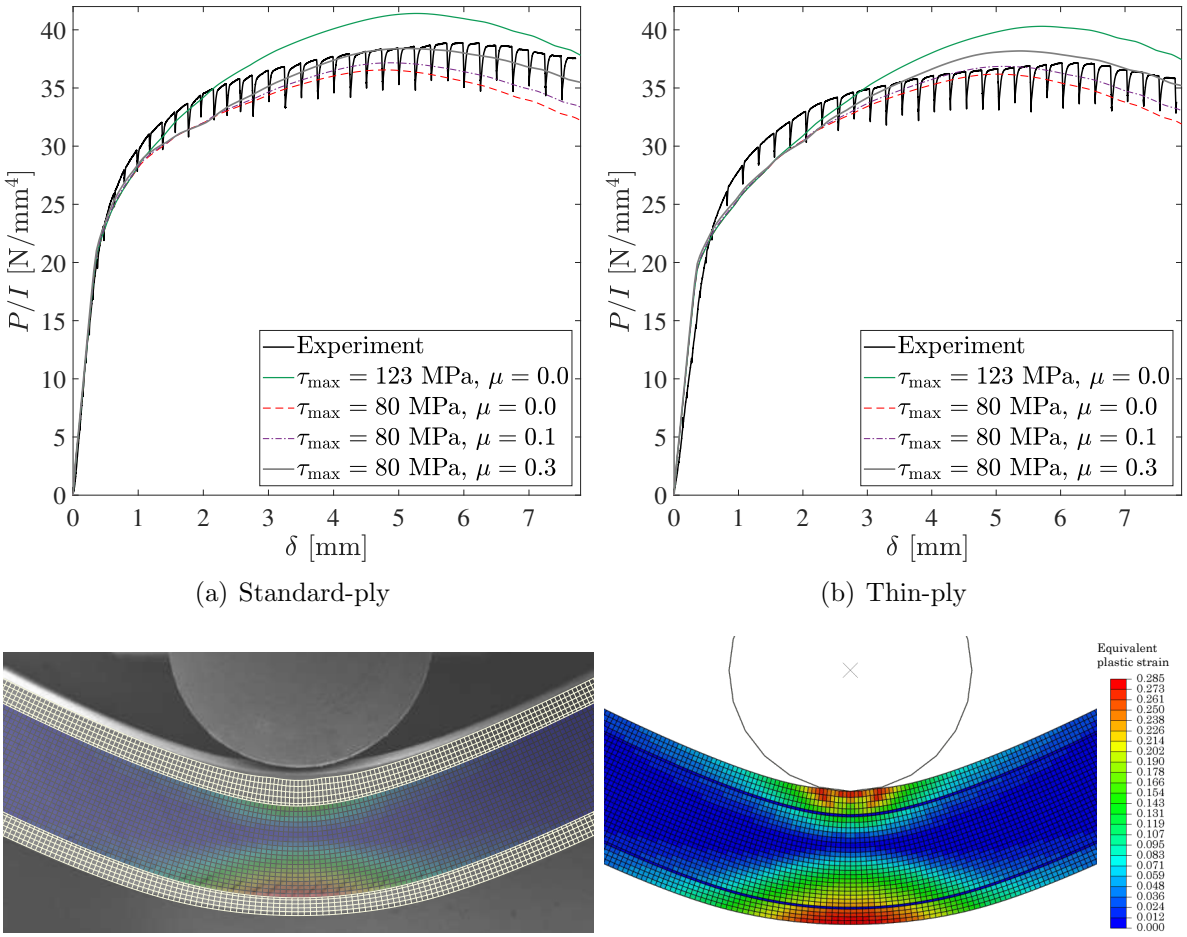

(a) Standard-ply

(b) Thin-ply

(c) The dissipated energy density (at the end of the test of the standard-ply model with $\tau_{\max} = 123\,\text{MPa}$) correlates well with the visible distributed damage.

(d) The equivalent plastic strain distribution at the end of the simulation in the standard-ply model with $\tau_{\max} = 123\,\text{MPa}$

Figure 12: The experimental and numerical results of the three-point bend tests on the hybrid aluminium/CFRP microstructures.

The equivalent plastic strain at the end of the simulation in the standard-ply microstructure with a shear strength $\tau_{\max} = 123\,\text{MPa}$ if given in Figure 12(d). The FE predicts diffuse plasticity under the load pin, with the most plastic strain in the aluminium on the tension side. Note that, despite the good predictions in Figures 12(a) and (b), the model, the model is relatively simple, as it does not represent explicitly the complex 3D nature of the microstructure, the failure mechanisms in the CFRP (e.g. splitting along the fibre direction) nor the ultimate failure of the various materials.

5. Conclusions

This paper investigated the first ever biomimetic hybrid metal/crossed-lamellar composite in order to achieve a microstructure that retains its structural integrity during bending up to very large applied curvatures. It can be concluded that:

- two possible microstructures were successfully prototyped using two different families of prepreg (standard-ply and thin-ply), both exhibiting similar, unique, mechanical behaviour;
- both prototyped microstructures preserve their structural integrity up to record large curvatures upon bending, in comparison with other hybrid CFRPs and quasi-isotropic CFRPs;
- the microstructures dissipate energy stably and under nearly constant load through damage diffusion in the middle layer and plastic deformation of the aluminium;
- in the standard-ply microstructure, the post-mortem investigation indicated fibre kinking near the ply interfaces, diffuse fibre failure and splits along the fibre direction – mechanisms that have not been reported before for crossed-lamellar microstructures;
- in the thin-ply microstructure, the post-mortem investigation indicated broken fibres, but no splits along the fibre direction due to higher in-situ transverse and shear strengths.

In summary, this paper presented the first hybrid aluminium/CFRP with a crossed-lamellar microstructure in the literature, and demonstrated that this configuration preserves its structural integrity up to significantly larger applied curvatures than any other hybrid with CFRP in the literature. The hybrid composite presented here therefore has potential for step changes in the design of applications where damage tolerance is the driver for design. The results also encourage further research into these type of microstructures and into the related prototyping methods to allow larger-scale manufacturing.

Acknowledgments

The funding from the EPSRC under the grant EP/M002500/1 is gratefully acknowledged. The authors also acknowledge Dr Bamber Blackman, from the Department of Mechanical Engineering at Imperial College London, for his kind and helpful assistance with the surface treatment of the aluminium.

References

[1] G. Bullegas, S. T. Pinho, and S. Pimenta. Engineering the translaminar fracture behaviour of thin-ply composites. *Composites Science and Technology*, 131:110–122, 2016.

[2] F. Narducci and S.T. Pinho. Exploiting nacre-inspired crack deflection mechanisms in CFRP via micro-structural design. *Composites Science and Technology*, 153:178–189, 2017.

[3] F. Narducci, K.-Y. Lee, and S.T. Pinho. Interface micro-texturing for interlaminar toughness tailoring: a film-casting technique. *Composites Science and Technology*, 156:203–214, 2018.

[4] R. Häsä and S.T. Pinho. Failure mechanisms of biological crossed-lamellar microstructures applied to synthetic high-performance fibre-reinforced composites. *Journal of the Mechanics and Physics of Solids*, 125:53–73, 2019.

[5] P.-Y. Chen, J. McKittrick, and M. A. Meyers. Biological materials: functional adaptations and bioinspired designs. *Progress in Materials Science*, 57(8):1492–1704, 2012.

[6] X. W. Li, H. M. Ji, G. P. Zhang, and D. L. Chen. Mechanical properties of crossed-lamellar structures in biological shells: A review. *Journal of the Mechanical Behavior of Biomedical Materials*, 74:54–71, 2017.

[7] J. D. Currey and A. J. Kohn. Fracture in the crossed-lamellar structure of Conus shells. *Journal of materials Science*, 11(9):1615–1623, 1976.

[8] N. M. Neves and J. F. Mano. Structure/mechanical behavior relationships in crossed-lamellar sea shells. *Materials Science and Engineering: C*, 25(2):113–118, 2005.

[9] Y. Liang, J. Zhao, L. Wang, and F.-M. Li. The relationship between mechanical properties and crossed-lamellar structure of mollusk shells. *Materials Science and Engineering: A*, 483:309–312, 2008.

[10] H. M. Ji, W. Q. Zhang, X. Wang, and X. W. Li. Three-point bending fracture behavior of single oriented crossed-lamellar structure in Scapharca broughtonii shell. *Materials*, 8(9):6154–6162, 2015.

[11] H. M. Ji, X. W. Li, and D. Chen. Cymbiola nobilis shell: Toughening mechanisms in a crossed-lamellar structure. *Scientific reports*, 7(40043):1–10, 2017.

[12] H. M. Ji, Y. Jiang, W. Yang, G. P. Zhang, and X. W. Li. Biological selfarrangement of fiber like aragonite and its effect on mechanical behavior of Veined rapa whelk shell. *Journal of the American Ceramic Society*, 98(10):3319–3325, 2015.

[13] H. M. Ji, W. Q. Zhang, and X. W. Li. Fractal analysis of microstructure-related indentation toughness of Clinocardium californiense shell. *Ceramics International*, 40(5):7627–7631, 2014.

[14] V. J. Laraia and A. H. Heuer. Novel composite microstructure and mechanical behavior of mollusk shell. *Journal of the American Ceramic Society*, 72(11):2177–2179, 1989.

[15] L. T. Kuhn-Spearing, H. Kessler, E. Chateau, R. Ballarini, A. H. Heuer, and S. M. Spearing. Fracture mechanisms of the Strombus gigas conch shell: implications for the design of brittle laminates. *Journal of Materials Science*, 31(24):6583–6594, 1996.

[16] A. Y.-M. Lin, M. A. Meyers, and K. S. Vecchio. Mechanical properties and structure of Strombus gigas, Tridacna gigas, and Haliotis rufescens sea shells: A comparative study. *Materials Science and Engineering C*, 26(8):1380–1389, 2006.

[17] R. Menig, M. H. Meyers, and K. S. Vecchio. Quasi-static and dynamic mechanical response of Strombus gigas (conch) shells. *Materials Science and Engineering A*, 297(1-2):203–211, 2001.

[18] L. Romana, P. Thomas, P. Bilas, J. L. Mansot, M. Merrifiels, Bercion Y., and D. Aldana Aranda. Use of nanoindentation technique for a better understanding of the fracture toughness of Strombus gigas conch shell. *Materials Characterization*, 76:55–68, 2013.

[19] C. L. Salinas, E. Escobar de Obaldia, C. Jeong, J. Hernandez, P. Zavattieri, and D. Kisalius. Enhanced toughening of the crossed lamellar structure revealed by nanoindentation. *Journal of the Mechanical Behavior of Biomedical Materials*, pages 1–11, 2017.

[20] X.-W. Su, D.-M. Zhang, and Heuer A. H. Tissue regeneration in the shell of the giant queen conch, Strombus gigas. *Chemistry of Materials*, 16(4):581–593, 2004.

[21] Y. A. Shin, S. Yin, X. Li, S. Lee, S. Moon, J. Jeong, M. Kwon, S. J. Yoo, Y.-M. Kim, T. Zhang, H. Gao, and S. H. Oh. Nanotwin-governed toughening mechanism in hierarchically structured biological materials. *Nature communications*, 7(10772):1–10, 2016.

[22] A. Osuna-Mascaró, T. Cruz-Bustos, S. Benhamada, N. Guichard, B. Marie, L. Plasseraud, M. Corneillat, G. Alcaraz, A. Checa, and F. Marin. The shell organic matrix of the crossed lamellar queen conch shell (Strombus gigas). *Comparative Biochemistry and Physiology Part B: Biochemistry and Molecular Biology*, 168:76–85, 2014.

[23] H. Zell. Eustrombus gigas. *https://upload.wikimedia.org/wikipedia/commons/9/9a/Eustrombus_gigas_01.jpg*, Used under CC-BY-SA-3.0: *https://creativecommons.org/licenses/by-sa/3.0/deed.en*, Accessed 13/12/2017.

[24] M. A. Meyers, P.-Y. Chen, A. Y.-M. Lin, and Y. Seki. Biological materials: Structure and mechanical properties. *Progress in Materials Science*, 53(1):1–206, 2008.

[25] G. Karambelas, S. Santhanam, and Z. N. Wing. Strombus gigas inspired biomimetic ceramic composites via SHELL - Sequential Hierarchical Engineered Layer Lamination. *Ceramics International*, 39(2):1315–1325, 2013.

[26] V. S. Kaul and K. T. Faber. Synthetic crossed-lamellar microstructures in oxide ceramics. *Journal of Ceramic Processing Research*, 6(3):218–222, 2005.

[27] L. Chen, R. Ballarini, H. Kahn, and A. H. Heuer. Bioinspired micro-composite structure. *Journal of Materials Research*, 22(1):124–131, 2007.

[28] D. F. Hou, G.S. Zhou, and M. Zheng. Conch shell structure and its effect on mechanical behaviors. *Biomaterials*, 25(4):751–756, 2004.

[29] G. X. Gu, M. Takaffoli, and M. J. Buehler. Hierarchically enhanced impact resistance of bioinspired composites. *Advanced Materials*, 29(1700060):1–7, 2017.

[30] C. L. Salinas. Multifunctional fiber-reinforced composites inspired by the shell of a bioluminescent marine gastropod. *PhD thesis, University of California, Riverside, CA, USA*, 2016.

[31] ASTM D7078/D7078M-12. Standard test method for shear properties of composite materials by V-notched rail shear method. *ASTM International, West Conshohocken, PA, USA*, 2012.

[32] T. Sinmazçelik, E. Avcu, M.Ö. Bora, and O. Çoban. A review: Fibre metal laminates, background, bonding types and applied test methods. *Materials & Design*, 32(7):3671–3685, 2011.

[33] G. W. Critchlow and D.M. Brewis. Review of surface pretreatments for aluminium alloys. *International Journal of Adhesion and Adhesives*, 16(4):255–275, 1996.

[34] G. S. Dhaliwal and G. M. Newaz. Experimental and numerical investigation of flexural behavior of carbon fiber reinforced aluminum laminates. *Journal of Reinforced Plastics and Composites*, 35(12):945–956, 2016.

[35] S. T. Pinho, R. Darvizeh, P. Robinson, C. Schuecker, and P. P. Camanho. Material and structural response of polymer-matrix fibre-reinforced composites. *Journal of Composite Materials*, 46(19-20):2313–2341, 2012.

[36] Hexcel. HexPly 8552 product data sheet, EU version. *http://www.hexcel.com/user_area/content_media/raw/HexPly_8552_eu_DataSheet.pdf*, Accessed 29/09/2017.

[37] Hexcel. HexPly 8552 product data sheet, US version. *http://www.hexcel.com/user_area/content_media/raw/HexPly_8552_us_DataSheet.pdf*, Accessed 29/09/2017.

[38] Y. He. Matrix-dominated constitutive laws for composite materials. *PhD thesis, Georgia Institute of Technology, GA, USA*, 2010.

[39] G. Czél and M. R. Wisnom. Demonstration of pseudo-ductility in high performance glass/epoxy composites by hybridisation with thin-ply carbon prepreg. *Composites Part A*, 52:23–30, 2013.

[40] J. D. Fuller and M. R. Wisnom. Exploration of the potential for pseudo-ductility in thin ply CFRP angle-ply laminates via an analytical method. *Composites Science and Technology*, 112:8–15, 2015.

[41] MatWeb. Alcald aluminium 2024-T3. *http://www.matweb.com/search/DataSheet.aspx?MatGUID=781ce4adb30c4d548320b0ab262a5d28*, Accessed 01/04/2019.

[42] J. Dogra. The development of a new compression test specimen design for thick laminate composites. *PhD thesis, Imperial College London, UK*, 2010.

Appendix A. Earlier configurations for the hybrid crossed-lamellar composites

Appendix A.1. Glass fibre/CFRP hybrid

The development of the hybrid crossed-lamellar microstructures was a lengthy process that required multiple iterations, during which the the microstructures were progressively improved based on the shortcomings identified in the previous iterations.

We investigated several configurations with different material systems in order to enhance the damage diffusion in the microstructures. First, we bonded glass fibre skins to a configuration that had three macroscopic crossed-lamellar CFRP layers with a $0°/90°/0°$ orientation (see Figure A.1(a)). The purpose of the skins was to provide cohesion for the tunnel cracks in order to facilitate damage diffusion in the inner layer and delay the failure of the middle layer. We used unidirectional stitched glass fibre with a thickness of $250\,\mu$m due to its lower stiffness and higher strain to failure compared with those of CFRP, and the fibre direction in the skins was perpendicular to the loading direction.

The configuration was tested in three-point bending in an SEM environment using a Deben Microtest Module with a 5 kN load cell. The results of the test are summarised in Figure A.1.

Only one tunnel crack was observed in the inner layer of the glass fibre/CFRP hybrid, followed by delamination at the inner/middle layer interface (Figure A.1(a)). Several deflected cracks subsequently grew in the middle layer, and the microstructure finally failed when the deflected cracks grew through the middle layer under the load pin (Figure A.1(b)). Furthermore, the skin on the compressive side delaminated from the outer layer and failed in compression.

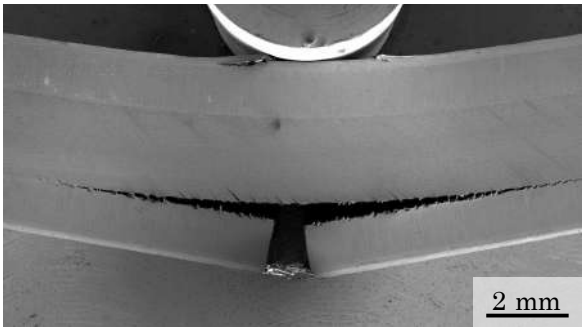

(a) Glass fibre/crossed-lamellar CFRP hybrid, early stage of the test

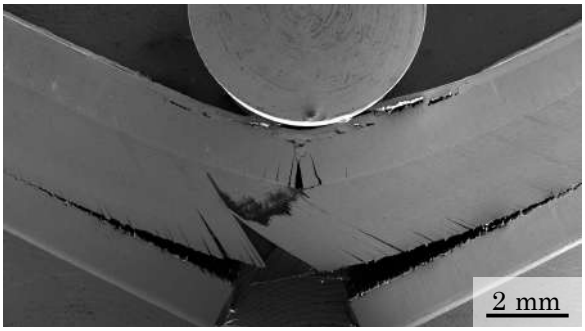

(b) Glass fibre/crossed-lamellar CFRP hybrid, end of the test

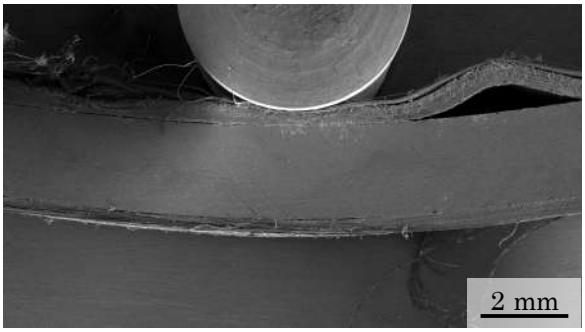

(c) UHMWPE/crossed-lamellar CFRP hybrid, early stage of the test

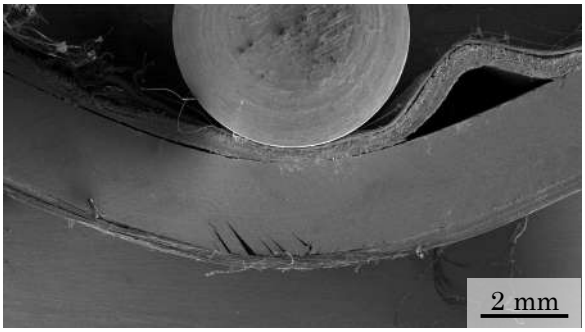

(d) UHMWPE/crossed-lamellar CFRP hybrid, end of the test

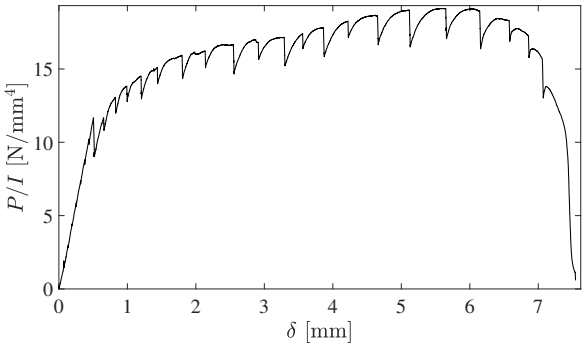

(e) Glass fibre/crossed-lamellar CFRP hybrid

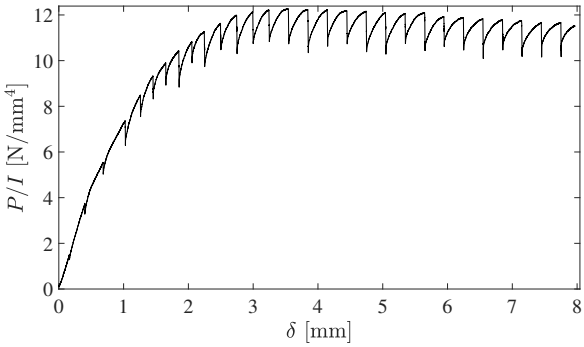

(f) UHMWPE/crossed-lamellar CFRP hybrid

Figure A.1: The hybrid crossed-lamellar microstructures were developed over several iterations.

The failure of the microstructure was dominated by damage accumulation, and eventual localisation, in the middle layer (Figure A.1(b)), which manifested as stable energy dissipation, as seen in the load vs displacement curve in Figures A.1(a), (b) and (e).

Appendix A.2. UHMWPE/CFRP hybrid

It was concluded from the hybrid glass fibre/CFRP configuration and from the results in Häsä and Pinho [4] that configurations with inner and outer layers made of crossed-lamellar CFRP lead to damage localisation. Furthermore, the glass fibre skins were not ductile and compliant enough to accommodate the large deformations of the crossed-lamellar microstructure, and they did not promote tunnel cracking in the inner layer. Therefore, the inner and outer layers of the crossed-lamellar CFRP were replaced by a 300 μm thick cross-ply of ultra-high-molecular-weight polyethylene (UHMWPE) prepreg that was bonded to the CFRP in a hot press.

The configuration was tested in three-point bending with in-situ SEM as the previous configuration. The test results are summarised in Figures A.1(c), (d) and (f).

Upon bending, the UHMWPE detached from the CFRP almost instantly (Figure A.1(c)), and as a consequence, did not offer much cohesion for deflected cracks that grew in the middle layer, leading these cracks to open on the tension side and advancing far into the middle layer (Figure A.1(d)).

The damage diffusion in the configuration occurred under stable conditions (see Figure A.1(f)), and, as the UHMWPE debonded at the initial stages of the test, the mechanical behaviour was governed by the response of the middle layer.

Appendix A.3. Discussion

The mechanical behaviour for both configurations, the glass fibre/CFRP hybrid and the UHMWPE/CFRP hybrid, was dominated by the response of the crossed-lamellar CFRP middle layer, yielding qualitatively similar load vs displacement curves (Figures A.1(e) and A.1(f)). In both cases, the damage occurs under stable conditions and the specimens could be loaded up to large displacements.

Therefore, it can be gleaned from the results of the early iterations of the hybrid crossed-lamellar composites presented in this appendix, and from the results presented in the main body of this paper, that the stable mechanical behaviour under nearly constant load is repeatable and characteristic for crossed-lamellar CFRPs.

The configurations presented in this appendix did not, however, prevent the cracks from opening and the damage from localising. In order to enhance the damage diffusion in the microstructure, we sought alternative materials for the inner and outer layers, leading to the development of the hybrid metal/crossed-lamellar composite presented in the main body this paper.